Spontaneous exciton dissociation at organic semiconductor interfaces facilitated by the orientation of the delocalized electron-hole wavefunction

Tika R. Kafle,[1] Bhupal Kattel,[1] Shanika Wanigasekara,[1] Ti Wang,[2] Wai-Lun Chan[1, *]

[1] Department of Physics and Astronomy, University of Kansas, Lawrence, KS 66045

[2] School of Physics and Technology, Center for Nanoscience and Nanotechnology, and Key Laboratory of Artificial Micro- and Nano-structures of Ministry of Education, Wuhan University, Wuhan 430072, China

[*] Corresponding author: wlchan@ku.edu

Abstract:

In organic semiconductors, optical excitation does not necessarily produce free carriers. Very often, electron and hole are bound together to form an exciton. Releasing free carriers from the exciton is essential for the functioning of photovoltaics and optoelectronic devices, but it is a bottleneck process because of the high exciton binding energy. Inefficient exciton dissociation can limit the efficiency of organic photovoltaics (OPV). Here, we determine nanoscale features that can allow the free carrier generation to occur spontaneously despite it is an energy uphill process. Specifically, by comparing the dissociation dynamics of the charge transfer (CT) excitonat two donor-acceptor interfaces, we find that the relative orientation of the electron and hole wavefunction within a CT exciton plays an important role in determining whether the CT exciton will decompose into the higher energy free electron-hole pair or relax to the lower energy tightly-bound CT exciton. We combine the concept of the entropic driving force with the structural anisotropy of typical organic crystals to devise a framework that can allow us to understand how the orientation of the delocalized electronic wavefunction can be manipulated to favor the energy-uphill spontaneous dissociation of CT excitons over the energy-downhill CT exciton cooling.

1. INTRODUCTION

Generation of free carriers from excitons is a multistep process that is usually initiated by the charge transfer at the donor-acceptor interface (also known as the type-II heterostructure), which results in the formation of Coulombic-bound CT excitons. These CT excitons have a binding energy of ~ 0.1 – 0.5 eV.[1, 2] How the bound CT exciton can be dissociated effectively into free carriers has been a long standing issue.[3-6] Various driving force such as entropy,[4, 7-9] vibronic coupling[10] and potential energy gradient created by the molecular mixing at the interface[11-14] have been proposed, which would facilitate the charge separation (CS). Kinetically, it is proposed that transient hot CT excitons that have excess energy can decompose directly into free carriers before they relax into lower energy CT excitons such that any energy uphill process can be avoided.[4, 15-17] However, this hot-CT exciton dissociation pathway remains controversial because a number of works have found that free carriers can be generated effectively by the absorption of sub-bandgap photons.[18-20] To further complicate this issue, the dissociation mechanism would depend strongly on the microstructure[21] and the dielectric environment[22] at the interface. Due to the anisotropic nature of organic crystals, the CS pathway should depend critically on the molecular packing at the interface. Unfortunately, in most spectroscopic studies, bulk-heterojunction (BHJ) samples are used in order to enhance the signal originated from interfaces. Because the resultant signal is originated from an ensemble of interfaces which can have different molecular orientations, correlating the dynamics with the structure remains a challenge.

Some earlier works on fullerene acceptors have suggested that free carriers can be generated directly from hot, delocalized CT excitons on a sub-ps timescale.[15, 23-29] These interfaces usually have a relative large interfacial energy offset such that the direct charge generation from hot CT excitons is an isoenergetic process. Interestingly, recent works on non-fullerene acceptors (NFAs) show that CT excitons can convert efficiently into free carriers despite

the much smaller energy offset at the donor-acceptor interface.[30-33] The small energy offset implies that CS is likely to be an energy uphill process because the singlet exciton has an energy lower than that of the free electron-hole pair. Hence, it is unclear why the energy uphill process can occur with such a high yield. The efficient CS can reduce the recombination of CT excitons, which can minimize the energy loss associated with the charge generation.[34-36] Therefore, identifying the mechanism on how effective CS process can occur will be the next crucial step for boosting the photovoltaic performance. Here, we address this issue by studying the CT exciton dissociation dynamics at bilayer donor-acceptor samples with well-defined molecular orientations. Enabling this study is a time-resolved two-photon photoemission spectroscopy (TR-TPPE) technique, which can spectrally resolve CT states with different binding energies.[29, 37] Using the technique, an energy uphill CT exciton dissociation process, with an energy increase of ~ 0.3 eV, is found to occur in ~ 10 ps at the zinc phthalocyanine (ZnPc)/F_8ZnPc model interface. This CT exciton dissociation rate is ~ 2 orders of magnitude faster than the Arrhenius rate calculated using the observed energy barrier. The observed dynamics resembles the characteristics of those found in BHJs consisting of NFAs.[38, 39] For example, no cooling of the CT exciton generated from the initial CT process is observed.[38] The CS process is fast compared to the thermally-activated dissociation of bound CT excitons, but it is slow compared to the direct and long range CS via hot and delocalized CT excitons.[25]

The results obtained from the ZnPc/F_8ZnPc interface is further compared to those obtained from the ZnPc/fullerene (C_{60}) interface. At the former interface, both the electron acceptor, F_8ZnPc, and donor, ZnPc, are planar molecules and they have a face-on orientation with respect to the interface. At the latter interface, ZnPc molecules with an edge-on orientation are grown on the isotropic C_{60} crystal. In contrast to the ZnPc/F_8ZnPc interface, a more conventional CS pathway is observed for the ZnPc/C_{60} interface. At ZnPc/C_{60}, the hot delocalized CT excitons first

relax into lower energy CT excitons in ~ 2 ps. Then, the cold CT excitons dissociate on the nanosecond (ns) timescale with a rate that is consistent with the slow Arrhenius rate. By using a model that combines the idea of the entropic driving force, the electron delocalization and the anisotropy of the organic crystal, we explain why the energy barrier for CT exciton dissociation can be overcome more readily at ZnPc/F_8ZnPc as compared to ZnPc/C_{60}. To our knowledge, although the entropic driving force have been invoked in previous works,[4, 7-9] constraints imposed on the electron delocalization by the crystal anisotropy have not been taken into consideration. We will further argue that the long-standing debate on whether CT excitons dissociate *via* hot or cold CT excitons would be an impropriate premise, but the key question should be on whether spontaneous exciton dissociation or hot exciton cooling is the preferred reaction direction after accounting for the entropic driving force. Moreover, we distinguish our work from other orientation dependent studies in which properties such as the electronic coupling and the interfacial CT rate,[40, 41] band alignment,[42] transport[43] and device efficiency[44, 45] are investigated. Electron delocalization that involves a group of molecules are rarely measured directly and its role on exciton dissociation is still under debate.

2. RESULTS AND DISCUSSION

Spontaneous dissociation of CT excitons at interfaces with a face-on molecular orientation

We will first discuss the results obtained from the ZnPc/F_8ZnPc interface in which the spontaneous dissociation of CT excitons is observed. ZnPc and F_8ZnPc molecules are grown on a highly ordered pyrolytic graphite (HOPG) substrate on which they are expected to have a face-on orientation.[46] Because face-on and edge-on molecules show different ionization potentials (IP),[47, 48] we can verify the face-on orientation of the ZnPc and F_8ZnPc molecules by measuring their IP (supporting information, Sec. I). As a result of the face-on orientation, both the electron and the hole wavefunction in the CT exciton delocalize along the direction that is perpendicular to the

interface (Fig. 1a). In term of the band alignment, the F_8ZnPc molecule has a larger IP as compared to the ZnPc while their optical band gaps are similar.[49] Hence, the F_8ZnPc-ZnPc interface has a type-II band alignment with the F_8ZnPc and the ZnPc acting as the electron acceptor and donor respectively. The highest occupied molecular orbital (HOMO) positions of ZnPc and F_8ZnPc of our sample are determined using ultraviolet photoemission spectroscopy (UPS). The UPS spectra for F_8ZnPc films with various thicknesses that are grown on a 10 nm-ZnPc film are shown in Fig. 1b. The HOMO-offset at the interface was found to be ≈ 0.45 eV and the HOMO shifts to a slightly lower energy as the F_8ZnPc thickness increases. The HOMO positions, together with the excited-states energy, as a function of the F_8ZnPc thickness are shown in Fig. 1c. The energies for the CT and CS states are measured by the TR-TPPE, which will be discussed in the next paragraph.

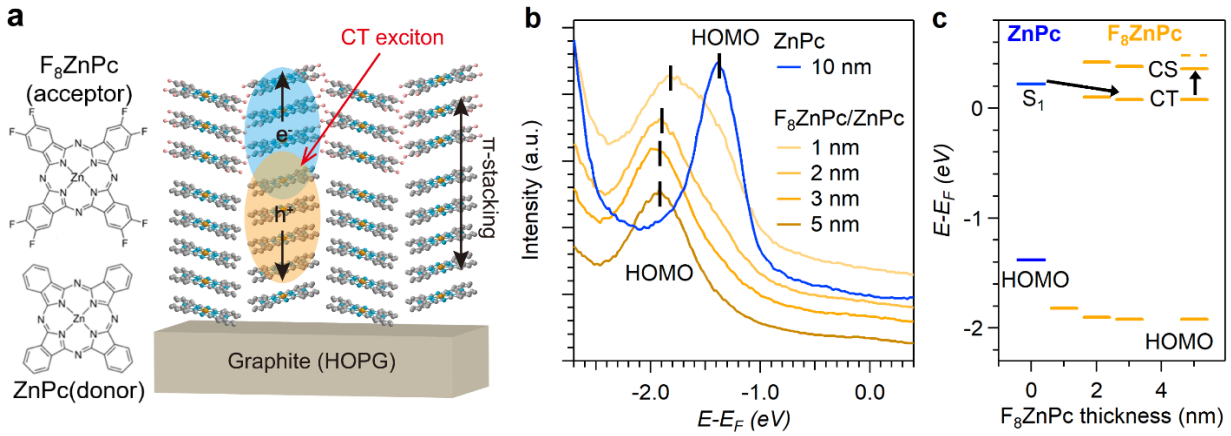

Figure 1: (a) A schematic diagram shows the F_8ZnPc/ZnPc interface. Both F_8ZnPc and ZnPc molecules grow on the HOPG substrate with a face-on orientation. As a result of this orientation, the electron and hole wavefunctions within the CT exciton are delocalized in a direction that is perpendicular to the interface. (b) UPS spectra for a 10 nm ZnPc sample and F_8ZnPc on 10 nm-ZnPc samples with various F_8ZnPc thicknesses. The F_8ZnPc thickness is shown in the figure legend. The HOMO peaks for ZnPc and F_8ZnPc are marked by the vertical bars (c) The energy level diagram at the F_8ZnPc/ZnPc interface. The positions of the HOMO and the CS/CT states are determined by our UPS and TR-TPPE experiments, respectively. The dashed lines indicate the positions of the edge of the LUMO state reported in the literature.

Figure 2a shows the TR-TPPE spectrum for a 5 nm-F_8ZnPc/10 nm-ZnPc sample. The pseudocolor represents the photoemission intensity. The *x*- and *y*- axis represent the time and the electron energy, respectively. We emphasis that the photoemission technique measures the energy

position of excited states, but not the optical transition energy. In the spectrum, the excited state energy is referenced with respect to the F_8ZnPc's HOMO measured by the UPS. Further information on how to understand the energy scale on the TPPE spectrum can be found in Ref. [50]. The pump photons excite the singlet (S_1) exciton in both ZnPc and F_8ZnPc. However, only excited electrons near the surface of the F_8ZnPc film is probed by the photoemission because of the limited escape depth (~ a few nm) of photoelectrons.[51] The intensity near the time-zero is attributed to the photoexcited S_1 exciton in F_8ZnPc. As shown in Fig. 2b, a similar spectral feature near the time-zero is also observed in the 15 nm F_8ZnPc/HOPG sample. Similar to the S_1 exciton in ZnPc,[29, 52] photoexcited S_1 exciton in F_8ZnPc is expected to relax in energy within hundreds of fs. From our previous studies on ZnPc, [29, 52] the relaxed F_8ZnPc's S_1 exciton should have a peak centered at ~ 1.6 eV relative to its HOMO level (or ~ 4.8 – 4.9 eV below the vacuum level), which falls outside of the spectral range that can be detected by our 4.68 eV probe photons. Hence, the signal becomes much weaker as the S_1 peak is shifting away from the detectable spectral range, which explains the rapid intensity decay in the first few hundreds fs after the pump excitation.

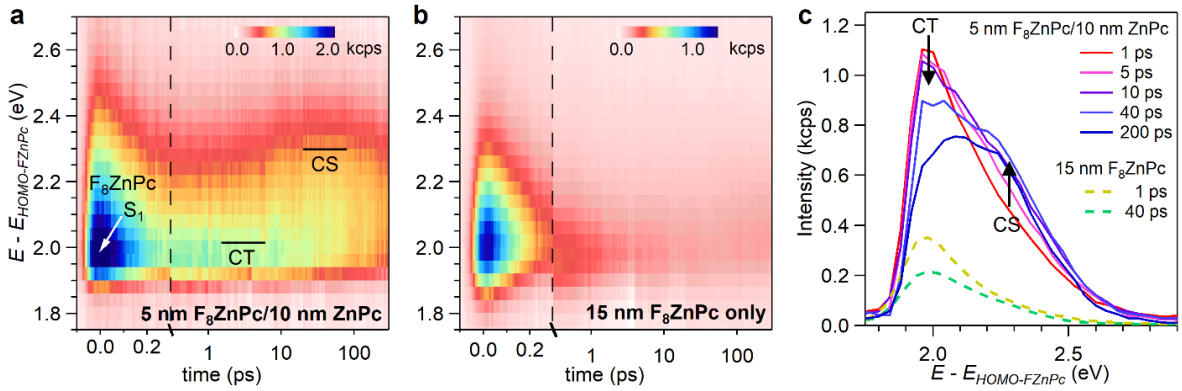

Figure 2: The TR-TPPE spectra for a (a) 5 nm-F_8ZnPc on 10 nm-ZnPc bilayer film and (b) a 15 nm-F_8ZnPc single-layer film. The plot is split by the vertical dashed line to show the dynamics on different timescales. (c) The TR-TPPE spectra at selected pump-probe delay times for the two samples. For the F_8ZnPc/ZnPc sample, the intensity of the bound-CT state and the charge-separated (CS) state decreases and increases with time, respectively. These states are not observed in the F_8ZnPc-only sample (dashed lines).

The major difference between the spectra of the F_8ZnPc/ZnPc and the F_8ZnPc samples is that long-lived signals (> 1 ps) in the spectral range of ~ 1.9 – 2.6 eV above the F_8ZnPc's HOMO are observed in the bilayer sample, but not in the F_8ZnPc sample (the right side of Fig. 2a and b). The spectra at selected pump-probe delay times are shown in Fig. 2c. Two states at ~ 2.0 eV and ~ 2.3 eV can be identified. Because these strong photoemission signals only show up in the spectrum of the bilayer sample, they are attributed to the CT at the donor-acceptor interface. The lower energy state is located at ~ 2.0 eV above the F_8ZnPc's HOMO, which is at an energy position higher than that of the F_8ZnPc's S_1 state (~ 1.7 eV). However, it is ~ 0.1 eV below the ZnPc's S_1 state (see Fig. 1c). Hence, the electron transfer from the ZnPc's S_1 to the state at ~ 2.0 eV is an energy downhill process. This peak is assigned to an interfacial CT state. Accounting for the interfacial HOMO offset of ~ 0.45 eV, the CT exciton energy is ~ 1.55 eV. The position of the higher energy peak (2.3 eV) is very close to the position of the edge of the F_8ZnPc's lowest unoccupied molecular orbital (LUMO) measured by inverse photoemission spectroscopy (IPES) studies (~ 2.4 eV above the HOMO peak position[53]) and it is assigned to the CS state. This pair of peaks can also be identified in spectra for samples with other F_8ZnPc's thicknesses (supporting information, Sec. II), although the CT (CS) state is less apparent in spectra obtained from samples with a thicker (thinner) F_8ZnPc layer. While we will focus on the dissociation of the CT exciton, we note that evidences for the initial electron transfer process from ZnPc to F_8ZnPc can be found in the spectra obtained from the 1 nm-ZnPc on F_8ZnPc sample. Similar to other donor-acceptor interfaces that we have studied using TR-TPPE,[29, 54-56] we observe a fast quenching in the ZnPc's S_1 signal on the 100-fs timescale (supporting information, Sec. IV) that is resulted from the CT from ZnPc to F_8ZnPc.

In Fig, 2c, it is apparent that the intensity of the CS state increases with time while the intensity of the CT state decreases. Hence, the overall spectral weight shifts towards a higher

energy. Moreover, we do not observe the CT exciton relaxes into other lower energy states (supporting information, Sec. II). Similar energy upshift is not observed in the spectra of the F_8ZnPc-only sample (dashed line in Figure 2c). The shifting of the overall spectral weight to a *higher* energy is a surprising observation because excited electrons usually relax to lower energy states on these ultrafast timescales (the Kasha's rule). Our result indicates that CT excitons are dissociated spontaneously, instead of relaxing to a lower energy state, after its creation. Similar dissociation dynamics is observed at 165 K (supporting information, Sec. III) although the intensity growth of the CS state is weaker. The conversion from the CT to the CS state is even more pronounced at a lower pump laser fluence (supporting information, Sec. III). Hence, this energy uphill process is not originated from an Auger-like exciton-exciton annihilation mechanism. Therefore, the CT exciton populated by the interfacial charge transfer can transform directly into the CS state without first relaxing to a lower energy CT state. As we will discuss, the dissociation of the CT exciton occurs at a rate ~ 2 orders of magnitude faster than the thermal activated rate calculated from the observed energy barrier (~ 0.3 eV). Hence, we will use the term spontaneous exciton dissociation (SED) to describe the observed energy uphill process.

Because photoemission is a surface sensitive probe, separated electrons generated at the buried ZnPc/F_8ZnPc interface cannot be detected until electrons reach the surface region of the F_8ZnPc layer. The concentration of separated carriers should also be lower in thicker samples because separated electrons generated from the interface can spread across a thicker F_8ZnPc layer. Hence, the intensity of the CS peak is expected to be weaker for samples with a thicker F_8ZnPc film. The maximum photoemission intensity reached by the CS peak as a function of the F_8ZnPc thickness is shown in Fig. 3a. As expected, the intensity decreases with the increase of the F_8ZnPc thickness. The temporal evolution of the integrated intensity of the CS peak is shown in Fig. 3b. For comparison, the intensity is normalized. The intensity reaches the maximum at an earlier time

for samples with a thinner F_8ZnPc layer. The time at which the intensity reaches its maximum is plotted as a function of the F_8ZnPc thickness in Fig. 3c (blue circle). The time constant, τ_{trans}, represents the time taken for separated electrons to transport from the ZnPc/F_8ZnPc interface to the surface of the film.

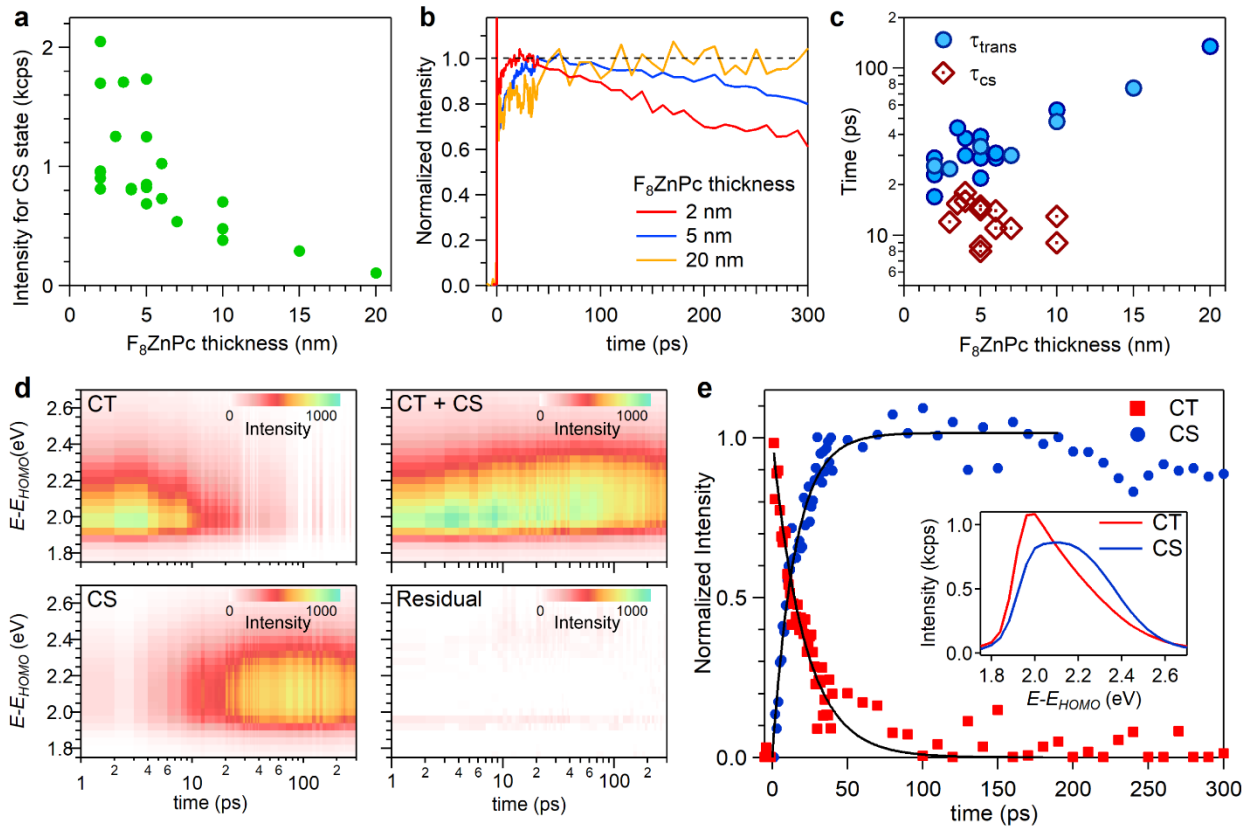

Figure 3: (a) The maximum photoemission intensity at the spectral range corresponding to the CS state as a function of the F_8ZnPc thickness. (b) The normalized intensity of the CS state as a function of time for three different F_8ZnPc thicknesses. The intensity reaches its maximum at a later time for larger F_8ZnPc thicknesses because of the time taken for electrons to transport from the ZnPc/F_8ZnPc interface to the surface of the F_8ZnPc film. (c) The time constants related to the electron transport time across the F_8ZnPc film (τ_{trans}) and the charge separation time (τ_{cs}) as a function of the F_8ZnPc thickness. (d) The fit spectrum for the data (Fig. 2a) of the 5 nm-F_8ZnPc/ZnPc sample for delay times $\geq$ 1 ps. The total spectrum is decomposed into two peaks: the CT and CS states. (e) The temporal evolution of the normalized intensity of the CT and CS peaks obtained from the fit. The dynamics are fit with a single exponential function (solid lines). The time constants of the exponential rise/decay correspond to the charge separation time. The inset shows the spectral shape for the CT and CS states used in the fit.

While the temporal evolution of the signal intensity shows that the separated electrons are drifting towards the surface of the F_8ZnPc layer, the shifting of the spectral weight to a higher

energy represents the dissociation of CT excitons into free carriers. In order to quantify the rate of the spectral shift, we decompose the spectrum in Fig. 2a into two peaks. A lower energy peak resembles the spectrum at early times (< 1 ps), and a higher energy peak resembles the spectrum at large delay times (200 – 300 ps) when the spectral shape no longer changes with time. The two peaks are labelled as "CT" and "CS", even though we note that the "CS" peak would represent a mixture of CT excitons and CS electrons that are in dynamical equilibrium at large delay times. The spectral weight of the two peaks at each delay time (for $t > 1$ ps) is determined independently by performing a standard least-square fit to the experimental spectrum. Figure 3d shows the 2D plots of the fit intensity for the two peaks and their sum. The total intensity subtracted from the experimental data is the residual of the fit, which is also shown in Fig. 3d. The magnitude of the residue is less than 5% of total intensity across the full spectrum. The spectral shape and the intensity evolution of the two peaks are shown in Fig. 3e. Fitting the evolution of the CT/CS intensity to a single exponential decay/rise function (solid lines in Fig. 3e) yields very similar time constants (CT: 21 ps/CS: 15 ps). This time constant quantifies how fast the electron gains its energy and it is attributed to the charge separation time τ_{cs}. The same fitting procedure is applied to spectra collected from samples with different F_8ZnPc thicknesses except for the 15 nm and 20 nm samples in which the CT peak cannot be clearly identified. The time constants τ_{cs} obtained from the exponential rise of the CS peak are shown in Fig. 3c (red diamond). Although we will not compare the magnitude of τ_{trans} and τ_{cs} directly, they show very different thickness dependences. Unlike τ_{trans}, τ_{cs} is less sensitive to the film thickness. Indeed, it has a somewhat smaller value for larger F_8ZnPc's thickness, which indicates that a thicker F_8ZnPc layer (i.e. more delocalization) favors the SED. The fast SED rate ($\sim 10^{11}$ s^{-1}) is fundamentally interesting. For an energy uphill process of ~ 0.3 eV (the observed energy different between the CS and CT states), the Arrhenius rate is on

the order of 10^9 s^{-1} (taking a pre-factor of 10^{14} s^{-1} [57]). Hence, the SED rate is ~ 2 orders of magnitude faster than the rate expected for a classical Arrhenius process.

Finally, the SED process observed at F_8ZnPc/ZnPc possesses features that are similar to the CS process observed in NFA-BHJs. First, all these interfaces have a relative small energy offset at the donor-acceptor interface, implying CS is an energy uphill process. Second, the small red-shift between the optical absorption and emission edges observed in NFA-BHJs[38] is consistent to the absence of the CT exciton cooling observed at the F_8ZnPc/ZnPc interface. The lack of CT exciton cooling can be explained by a strong mixing between the S_1 and CT exciton state.[38] Third, the timescale (~ 10 ps) for free carrier generation is similar to those observed in NFA-BHJs.[38, 39]

Hot CT Exciton Cooling at interfaces with an edge-on molecular orientation

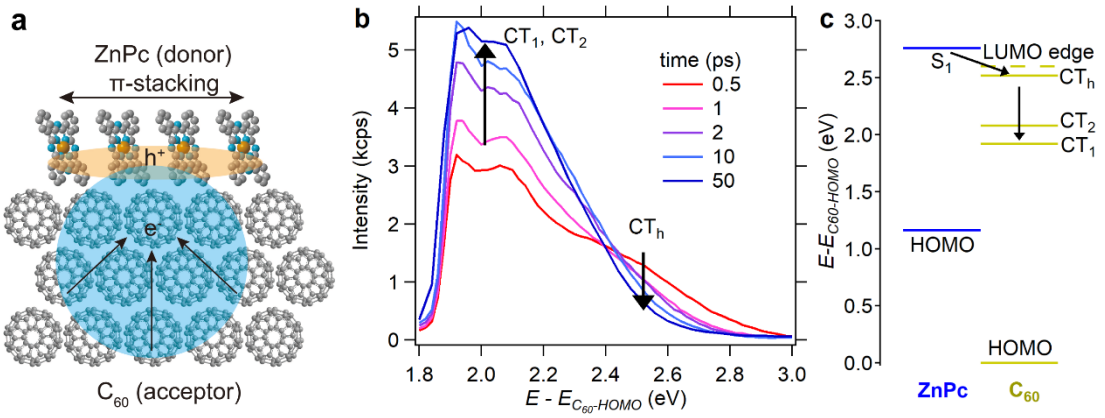

Figure 4: (a) A schematic diagram shows the orientation of molecules at the ZnPc/C_{60} interface used in our experiment. (b) The TR-TPPE spectra obtained from a 1 nm-ZnPc/4 nm-C_{60} sample at selected delay times. Unlike the F_8ZnPc/ZnPc interface, the intensity of the lower energy CT_1, CT_2 peaks increases as the intensity of the higher energy CT_h peak decreases. (c) The energy level diagram of the ZnPc/C_{60} interface.

For comparison, we note that the SED, which is an energy uphill process, is not a universal behavior. Indeed, it is commonly observed or presumed that hot CT excitons first relax into bound ones on the ultrafast (fs – ps) timescale. Then, bound CT excitons dissociate through thermal activated processes. For example, our previous TR-TPPE work found that hot CT exciton cooling instead of SED occurs at the ZnPc/C_{60} interface.[29, 37] At this interface, ZnPc molecules have an

edge-on orientation relative to the interface (Fig. 4a), and hot delocalized CT excitons relax into localized ones in ~ 2 ps after its excitation. Spectrally, the cooling process results in a downshift in the CT exciton energy (i.e. an increase in the exciton binding energy), which is opposite of the energy upshift observed in Fig. 2. TR-TPPE spectra at selected delay times from the ZnPc/C_{60} sample are reproduced in Fig. 4b and more details can be found in Ref. [29]. Previously, we also found that the delocalization size of the CT exciton decreases when it relaxes from the higher energy CT_h state to the lower energy CT_1 and CT_2 states. Using a time-resolved photoelectrical technique, we found that uncombined CT_1 and CT_2 excitons can dissociate into free carriers in a few nanoseconds.[37, 58] The charge generation yield decreases significantly with the decrease in the temperature (supporting information, Sec. V). This observation suggests that after the initial hot CT exciton cooling, free carriers are formed by the slow-ns, thermal-activated dissociation of cold CT excitons at the ZnPc/C_{60} interface.

Figure 4c shows the energy level diagram of the ZnPc/C_{60} interface. Similar to the F_8ZnPc/ZnPc interface, the ZnPc's S_1 state has an energy that is very close to the LUMO edge of the acceptor molecule (dashed line in Fig. 1c and Fig. 4c). Indeed, the S_1 state of ZnPc is at an energy slightly higher than the C_{60}'s LUMO edge, which would favor the SED instead of the hot exciton cooling. Hence, the energy level alignment cannot explain the very different fates of the CT excitons observed in the two systems. Moreover, at the F_8ZnPc/ZnPc interface, the CS yield measured by our time-resolved photoelectrical method has a much weaker temperature dependence as compared to the ZnPc/C_{60} interface (supporting information, Sec. V). The weak temperature dependence of the CS yield implies that the SED is still fast as compared to the CT exciton recombination even at low temperatures, which in turn suggests a very small effective energy barrier for the SED process. However, a ~0.3 eV barrier is directly observed in our TP-TPPE spectrum (Fig. 2). This apparent discrepancy can be resolved by considering the reduction

in the free energy barrier originated from the entropic gain during the CS process, and the dependence of the entropy gain on the orientation of the delocalized electron wavefunction.

Electron delocalization and the density of state of the CT state manifold

We note that SED is an energy uphill process. Thermodynamically, an energy uphill reaction can occur spontaneously if the number of final states is much larger than the number of initial states so that the increase in the enthalpy can be compensated by the decrease in the free energy originated from the entropy gain. This is referred to as the entropic driving force in the literature.[4, 7-9] For CS, this condition would be fulfilled when tens to hundreds of molecules are electronically "linked" together, which can significantly increase the number of available CS states. Quantum mechanically, because of the electronic coupling between neighboring molecules, a discrete set of CT and CS states can be hybridized into a manifold of states with various energies. The number of available states per unit energy within this manifold can be described by an energy-dependent function known as the density of state (DOS). The number of available state at a certain energy corresponds to the number of configurations in the definition of the equilibrium entropy. Mathematically, the relationship between the entropy gain ΔS and the DOS as a function of energy E can be written as:

$$\Delta S(E) = S(E + \Delta E) - S(E) = k_B \ln\left(\frac{\mathrm{DOS}(E + \Delta E)}{\mathrm{DOS}(E)}\right)$$

, where k_B is the Boltzmann constant. Hence, if the DOS of loosely bound and high energy CT states is much larger than the DOS of tightly bound and low energy CT states, SED instead of hot exciton cooling would occur because of the larger entropy gain.

To illustrate how the DOS function depends on the orientation of the delocalized wavefunction, we model the DOS of the CT manifold using a generic tight-binding model. In this model, the CT exciton (in the site representation) is described by a two-body wavefunction $|i, j\rangle$,

where i and j represent the positions of electron and hole in the acceptor and donor crystals, respectively. If there are N and M sites in acceptor and donor crystals respectively, the total number of states will be $N \times M$. The Hamiltonian H for the CT states can then be written as:

$$H = \sum_{i}^{N}\sum_{j}^{M} V_c(i,j)|i,j\rangle\langle i,j| + \sum_{j}^{M}\sum_{i,n,i\neq n}^{N} J_{el}(n,i)\,|n,j\rangle\langle i,j| + \sum_{i}^{N}\sum_{j,m,j\neq m}^{M} J_h(m,j)\,|i,m\rangle\langle i,j|$$

In this Hamiltonian, $J_{el}(n, i)$ is the electron transfer integral between site n and site i in the acceptor crystal and $J_h(m, j)$ is the hole transfer integral between site m and site j in the donor crystal. We only consider the electronic coupling between the nearest neighbor sites that are along the π–stacking direction. The potential $V_c(i, j)$ represents the Coulomb interaction between electron and hole. The energies of all the eigenstates can then be determined by diagonalizing the Hamiltonian. Based on the anisotropy in the π-stacking direction, the ZnPc and F_8ZnPc crystals are modeled as a row of molecules[59] that is either perpendicular or parallel to the interface. The C_{60} crystal is modelled as an isotopic square lattice. The positions of molecules for the two interfaces are shown schematically in Fig. 1a and 4a, and quantitatively in Fig. 5. Detailed parameters of this model can be found in the method section. Similar models have been used by others[23, 60] to study exciton delocalization and CS.

Figure 5a shows the energy of eigenstates as a function of the average electron-hole separation, r, for the C_{60}/ZnPc (yellow) and the F_8ZnPc/ZnPc (purple) interfaces. Each dot on the plot represents a single eigenstate. On this plot, we can identify two different groups of states. The first group of states are band-like electronic states with r essentially limited by the system size (the size of the each crystal is set at ≈ 10 nm – see Fig. 5c). The band-like states at the F_8ZnPc/ZnPc interface have a slightly larger r than that at the C_{60}/ZnPc interface because of the geometric constraint imposed by the orientation of the row of ZnPc molecules, i.e. the free hole in ZnPc always locates closer to the acceptor crystal when it is orientated parallel to the interface. The

energy of these states ranges from ~0.2 to -0.2 eV. The spreading in energy (the band width) is resulted from the coupling between the neighboring molecules. For these band-like states, the binding energy originated from the Coulomb interaction is insignificant. Hence, these states represent the CS states. The second group of states are bound CT states. On Fig. 5a, these states collapse onto a line on which the energy decreases with decreasing r because the Coulomb potential is inversely proportional to the distance. To convert this distribution into the DOS function, we divide the energy axis into bins and the DOS is defined as the number of states within each energy bin normalized by the total number of eigenstates. The DOS functions for the two interfaces are shown in Fig. 5b. We note that the DOS is plotted on a log scale. Hence, the horizontal distance between two points on the plot is proportional to the change in the entropy (ΔS). For both interfaces, the number of band-like states are much larger than the number of bound-CT states. Hence, the SED process always results in increases in both entropy and energy.

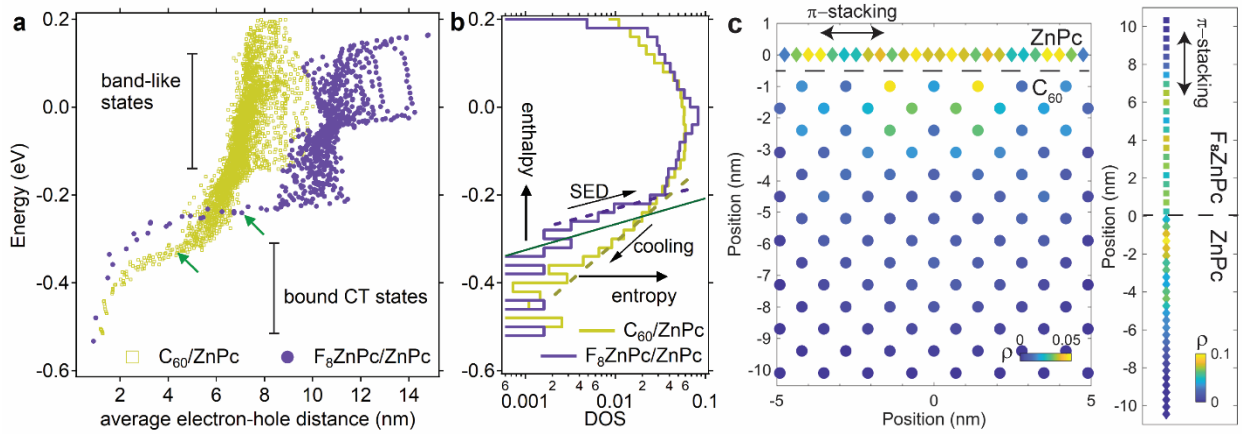

Figure 5: (a) The energies and average electron-hole distances for the eigenstates of the two interfaces, C_{60}/ZnPc and F_8ZnPc/ZnPc, determined by using the tight-binding model. (b) The DOS function for the two interfaces determined from the data shown in (a). The green solid line represents the critical slope for which $\Delta E = T\Delta S$ at room temperature. (c) The spatial distribution of the electron and hole densities for the two eigenstates marked by the green arrows in (a).

Despite the similarities, the C_{60}/ZnPc interface shows a larger DOS for bound-CT states (between – 0.2 eV and – 0.5 eV) as compared to the F_8ZnPc/ZnPc interface. More importantly, for

the F_8ZnPc/ZnPc interface, the entropy changes more rapidly as the energy (or enthalpy) of the CT state increases. In Fig. 5b, the ratio $\Delta E/\Delta S$ is proportional to the local slope of the DOS curve (dashed lines). The flatter the slope, the more likely that the SED process is favored. The slope of the C_{60}/ZnPc's curve (yellow dashed line) is ≈ 3.5 times of the slope of the F_8ZnPc/ZnPc's curve (purple dashed line). For reference, the slope at which $\Delta E = T\Delta S$ at room temperature is indicated by the green solid line. For the F_8ZnPc/ZnPc interface, the local slope of the DOS function is comparable to the slope of the green line. Hence, the entropic driving force can fully compensate the increase in the enthalpy, which allows the SED process to occur. On the other hand, for the C_{60}/ZnPc interface, the decrease in the free energy due to the entropy gain is not enough to compensate the increase in the enthalpy because the local slope of the DOS curve is steeper. Therefore, the reverse process, the hot CT exciton cooling, is preferred. This is consistent with our experimental observation. We note that the slope of the DOS curve does not change significantly when the simulation size is further increased to 15 nm (supporting information, Sec. VI).

More physical insight can be obtained by visualizing the spatial distribution of the electron density of CT states that have energies close to the bottom of the CS band. In Fig. 5a, these states are located at the kink between the group of band-like states and the line of bound CT states. A CT state for each interface is chosen randomly near the kink, which is identified by the green arrows in Fig. 5a. Figure 5c shows the spatial distribution of the electron and hole density ρ for the two CT states. The method for determining ρ is discussed in the supporting information – Sec. VII. The electron and hole within both CT states are relatively delocalized with comparable spatial sizes. However, as a result of the geometric constraint imposed by the π-stacking direction, the two states have rather different r and binding energies. For the ZnPc/C_{60} interface, because of the edge-on orientation of the ZnPc, the hole in ZnPc locates very close to the interface despite

delocalization. Moreover, the vicinity of the hole tends to pull the delocalized electron in the isotropic C_{60} crystal toward to the interface. These factors increase the exciton binding energy and reduce *r*. On the other hand, electron and hole delocalization at the ZnPc/F_8ZnPc interface push both electron and hole away from the interface because they both delocalize in a direction that is perpendicular to the interface. As a result, CT states formed at the ZnPc/F_8ZnPc interface generally have smaller binding energies and larger *r*. The geometric constraint affects the shape of the DOS curve, which in turn determine the reaction direction (SED versus hot exciton cooling).

3. CONCLUSION

Two major implications can be drawn from our study. First, it is commonly assumed that CT excitons dissociate through either the charge extraction from hot CT excitons before its relaxation (pathway 1 in Fig. 6a), or the thermal activated dissociation of cold CT excitons (pathway 2 in Fig. 6a). Many arguments on the CS mechanism in the literature are centered on whether the "hot" pathway or the "cold" pathway dominates the CS process.[3-6, 61, 62] Works that observe the ultrafast formation of free carriers or the presence of hot CT states are often used as evidences to support the "hot" pathway.[16, 17] On the other hand, the observation of effective charge generation with sub-bandgap photoexcitation supports the "cold" pathway.[18-20] We note that the "hot" versus "cold" argument (Fig. 6a) is based on an intrinsic assumption that hot CT excitons always relax spontaneously into cold CT excitons (the black arrow in Fig. 6a). This prevalent assumption is likely to be originated from the Kasha's rule, which is well-known in the area of photochemistry. However, this assumption is not necessarily true in the condensed phase because the free energy change originated from the entropy change can be large enough to compensate the enthalpy change, which can drive the reaction in an energy uphill direction, i.e. the SED. If the uphill SED is favored, it does not matter whether a hot or a cold CT state is populated initially because either of them would decompose spontaneously into free carriers.

Thereby, the charge generation yield will not depend on the photon energy, as found in a number of experimental studies.[18-20] However, this does not imply slow or inefficient CS because the free energy barrier for CS can be significantly reduced by the entropic contribution. As illustrated in Fig. 6b, the factor that determines the CS efficiency is which reaction direction, SED or hot exciton cooling, dominates once the CT exciton (either cold or hot) is formed. The reaction direction can be determined by the relative orientation of the delocalized electron and hole wavefunctions because it affects the shape of the DOS function of the CT manifold, and hence $S(E)$. As a result, the charge generation yield is expected to depend sensitively on the morphology of the donor-acceptor blend, which can explain why a wide range of seemingly contradictory behaviors have been reported in the literature.

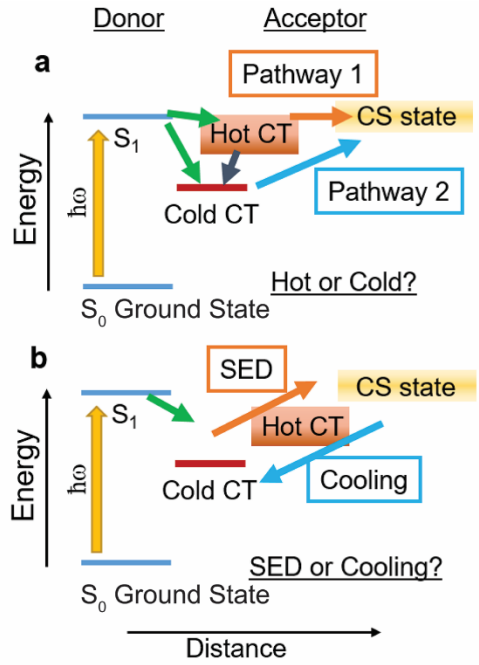

Figure 6: (a) An energy level diagram illustrating the "hot" and "cold" charge separation pathways that are commonly discussed in the literature. Significant efforts have been devolved to understand which pathway is dominant in the charge separation process. (b) Here, we suggest that the charge separation efficiency should depend on whether the SED process (forward reaction) or the hot CT exciton cooling (backward reaction) is the favorable reaction direction at a particular interface.

Second, recent advances in NFA OPVs result in a quantum jump in the OPV efficiency.[32, 33] Single-junction and tandem non-fullerene OPVs can have efficiencies as high as 15%[63] and 17%,[64] respectively. Interestingly, compared to fullerene OPVs, these NFA OPVs often have a large photocurrent (i.e. more effective exciton dissociation) despite of the relative small energy

offset at the donor-acceptor interface.[32, 33] This is rather surprising because a small energy offset can preclude the possibility for any isoenergetic CS pathway, which results in an energy uphill CS process. In light of our current work, we argue that employing planar acceptor and planar donor has the advantage in allowing both molecules to be oriented with a face-on orientation by the natural π-π interaction between donor and acceptor units. By contrast, for isotropic fullerenes, it is unavoidable in a typical BHJ that some donor domains will be oriented such that its π-stacking direction is parallel to the interface. Hence, the energy-uphill SED would occur more readily and robustly across different regions within a non-fullerene-based BHJ as compared to a fullerene-based BHJ, which can explain the efficient exciton dissociation in non-fullerene OPVs even with a small energy offset at the donor-acceptor interface.

EXPERIMENTAL SECTION

Sample Preparation

ZnPc (>99%, sublimed) and F_8ZnPc (>99%, sublimed) molecules were purchased from Luminescence Technology (Taiwan) and they were used as received. These molecules were deposited on a highly ordered pyrolytic graphite (HOPG) crystal. ZnPc molecules can be deposited on HOPG with a face-on orientation in a layer-by-layer fashion.[46] Prior to the deposition, the outer surface of the HOPG substrate was peeled off by using a scotch tape. The HOPG was then loaded into an ultrahigh vacuum (UHV) chamber with a base pressure of 1×10^{-9} Torr where it was annealed at 400 °C for 12 hours. A ZnPc film (10 nm) was first deposited on the HOPG substrate, which was followed by the F_8ZnPc film (2 nm – 20 nm). The deposition rate, which is monitored by a quartz crystal microbalance, was controlled in the range of 0.7–0.8 Å/min. The deposition was done at room temperature. After the deposition, the sample was transferred *in-situ* to another UHV chamber with a base pressure of 8×10^{-11} Torr, where ultraviolet photoemission spectroscopy (UPS) and time-resolved two photon photoemission spectroscopy (TR-TPPE) measurements were performed.

Photoemission experiment

The UPS measurement was done using the He-I emission line (21.22 eV) generated from a UV discharge lamp. The spectra were collected using a hemispherical electron analyzer (Phoibos 100, SPECS). In the TR-TPPE measurement, a pump laser pulse (1.77 eV, 25 fs) was used to excite the sample and a probe laser pulse (4.68 eV, 65 fs) was used to ionized the excited electrons. The aforementioned electron analyzer was used to measure the kinetic energy the ionized electrons. The pair of pump and probe pulses were generated from two non-collinear optical

parametric amplifiers (NOPA) (Orpheus-N-2H; Orpheus-N-3H, Light Conversion). Both NOPAs were pumped by a Yb:KGW regenerative amplifier running at 125 kHz (Pharos 10W, Light Conversion). The beam size had a full-width half-maximum (fwhm) of 0.8 mm at the sample.

Tight-binding model

For the Hamiltonian shown in the main text, the Coulomb potential is given by: $V_c(i,j) = -\frac{e^2}{4\pi\kappa\epsilon_0}\frac{1}{r_{i,j}}$, where ϵ_0 is the vacuum permittivity, κ is the dielectric constant, and $r_{i,j}$ is the distance between site i and site j. A dielectric constant equal to 3.5 was used, which is a typical value for organic semiconductors. The electron and hole transfer integral (J_{el}, J_h) between nearest neighbors was set to be 50 meV. This value is in line with typical values reported for phthalocyanine and fullerene crystals.[65-68] A single value was used so that the effect from the orientation can be studied. For the crystal structure, ZnPc and F_8ZnPc were modelled by a row of molecules with intermolecular spacing equal to 0.38 nm[59] and 0.48 nm,[67] respectively. For the distance between ZnPc and F_8ZnPc molecules at the interface, an average distance equal to 0.43 nm was used. For the C_{60} crystal, the distance between the planes was 0.7 nm (see Fig. 5c). This value was chosen based on a lattice constant of 1.4 nm for a face-centered cubic unit cell.[66] The distance between the ZnPc's and the C_{60}'s plane at the interface was set to be 1 nm, which is the average of the interplanar spacing between two rows of ZnPc molecules (~ 1.3 nm)[59] and the interplanar spacing of the C_{60} crystal (0.7 nm). The method for determining the average electron-hole distance of an eigenstate and the spatial distribution of the electron density is discussed in the supporting information, Sec. VII.

ACKNOWLEDGEMENTS

The work is supported by the U. S. National Science Foundation, Grant DMR-1351716. This investigation was partially supported by the University of Kansas General Research Fund allocation #2151080.

CONFLICT OF INTEREST

The authors declare no conflict of interest.

TOC FIGURE

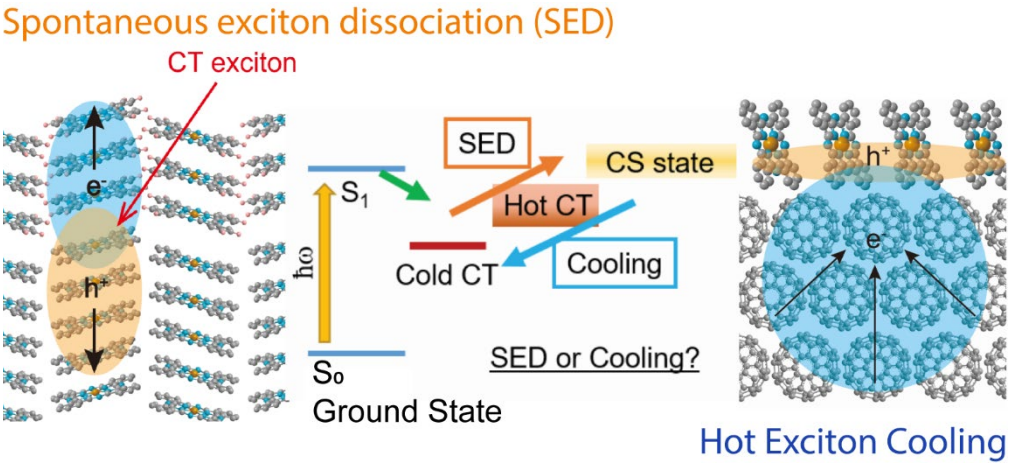

REFERENCES

[1] X. Y. Zhu, Q. Yang, M. Muntwiler, *Acc. Chem. Res.* **2009**, *42*, 1779.

[2] P. Merkl, F. Mooshammer, P. Steinleitner, A. Girnghuber, K. Q. Lin, P. Nagler, J. Holler, C. Schuller, J. M. Lupton, T. Korn, S. Ovesen, S. Brem, E. Malic, R. Huber, *Nat. Mater.* **2019**, *18*, 691.

[3] J. L. Bredas, J. E. Norton, J. Cornil, V. Coropceanu, *Acc. Chem. Res.* **2009**, *42*, 1691.

[4] T. M. Clarke, J. R. Durrant, *Chem. Rev.* **2010**, *110*, 6736.

[5] C. S. Ponseca, P. Chabera, J. Uhlig, P. Persson, V. Sundstrom, *Chem. Rev.* **2017**, *117*, 10940.

[6] O. Ostroverkhova, *Chem. Rev.* **2016**, *116*, 13279.

[7] Y. Yao, X. Y. Xie, H. B. Ma, *J. Phys. Chem. Lett.* **2016**, *7*, 4830.

[8] N. R. Monahan, K. W. Williams, B. Kumar, C. Nuckolls, X. Y. Zhu, *Phys. Rev. Lett.* **2015**, *114*, 247003.

[9] B. A. Gregg, *J. Phys. Chem. Lett.* **2011**, *2*, 3013.

[10] S. M. Falke, C. A. Rozzi, D. Brida, M. Maiuri, M. Amato, E. Sommer, A. De Sio, A. Rubio, G. Cerullo, E. Molinari, C. Lienau, *Science* **2014**, *344*, 1001.

[11] D. P. McMahon, D. L. Cheung, A. Troisi, *J. Phys. Chem. Lett.* **2011**, *2*, 2737.

[12] J. A. Bartelt, Z. M. Beiley, E. T. Hoke, W. R. Mateker, J. D. Douglas, B. A. Collins, J. R. Tumbleston, K. R. Graham, A. Amassian, H. Ade, J. M. J. Frechet, M. F. Toney, M. D. McGehee, *Adv Energy Mater* **2013**, *3*, 364.

[13] P. Westacott, J. R. Tumbleston, S. Shoaee, S. Fearn, J. H. Bannock, J. B. Gilchrist, S. Heutz, J. deMello, M. Heeney, H. Ade, J. Durrant, D. S. McPhail, N. Stingelin, *Energy Environ Sci* **2013**, *6*, 2756.

[14] T. M. Burke, M. D. McGehee, *Adv. Mater.* **2014**, *26*, 1923.

[15] B. M. Savoie, A. Rao, A. A. Bakulin, S. Gelinas, B. Movaghar, R. H. Friend, T. J. Marks, M. A. Ratner, *J. Am. Chem. Soc.* **2014**, *136*, 2876.

[16] A. E. Jailaubekov, A. P. Willard, J. R. Tritsch, W. L. Chan, N. Sai, R. Gearba, L. G. Kaake, K. J. Williams, K. Leung, P. J. Rossky, X. Y. Zhu, *Nat. Mater.* **2013**, *12*, 66.

[17] G. Grancini, M. Maiuri, D. Fazzi, A. Petrozza, H. J. Egelhaaf, D. Brida, G. Cerullo, G. Lanzani, *Nat. Mater.* **2013**, *12*, 29.

[18] J. Lee, K. Vandewal, S. R. Yost, M. E. Bahlke, L. Goris, M. A. Baldo, J. V. Manca, T. Van Voorhis, *J. Am. Chem. Soc.* **2010**, *132*, 11878.

[19] T. G. J. van der Hofstad, D. Di Nuzzo, M. van den Berg, R. A. J. Janssen, S. C. J. Meskers, *Adv Energy Mater* **2012**, *2*, 1095.

[20] K. Vandewal, S. Albrecht, E. T. Hoke, K. R. Graham, J. Widmer, J. D. Douglas, M. Schubert, W. R. Mateker, J. T. Bloking, G. F. Burkhard, A. Sellinger, J. M. J. Frechet, A. Amassian, M. K. Riede, M. D. McGehee, D. Neher, A. Salleo, *Nat. Mater.* **2014**, *13*, 63.

[21] S. D. Dimitrov, M. Azzouzi, J. Wu, J. Yao, Y. Dong, P. S. Tuladhar, B. C. Schroeder, E. R. Bittner, I. McCulloch, J. Nelson, J. R. Durrant, *J. Am. Chem. Soc.* **2019**, *141*, 4634.

[22] S. Chen, S. W. Tsang, T. H. Lai, J. R. Reynolds, F. So, *Adv. Mater.* **2014**, *26*, 6125.

[23] H. Vazquez, A. Troisi, *Phys. Rev. B* **2013**, *88*, 205304.

[24] H. Tamura, I. Burghardt, *J. Am. Chem. Soc.* **2013**, *135*, 16364.

[25] S. Gelinas, A. Rao, A. Kumar, S. L. Smith, A. W. Chin, J. Clark, T. S. van der Poll, G. C. Bazan, R. H. Friend, *Science* **2014**, *343*, 512.

[26] A. J. Barker, K. Chen, J. M. Hodgkiss, *J. Am. Chem. Soc.* **2014**, *136*, 12018.

[27] G. D'Avino, L. Muccioli, Y. Olivier, D. Beljonne, *J. Phys. Chem. Lett.* **2016**, *7*, 536.

[28] B. Bernardo, D. Cheyns, B. Verreet, R. D. Schaller, B. P. Rand, N. C. Giebink, *Nat. Commun.* **2014**, *5*, 3245.

[29] T. Wang, T. R. Kafle, B. Kattel, W.-L. Chan, *J. Am. Chem. Soc.* **2017**, *139*, 4098.

[30] S. M. Menke, A. Cheminal, P. Conaghan, N. A. Ran, N. C. Greehnam, G. C. Bazan, T. Q. Nguyen, A. Rao, R. H. Friend, *Nat. Commun.* **2018**, *9*, 277.
[31] Y. Tamai, Y. L. Fan, V. O. Kim, K. Ziabrev, A. Rao, S. Barlow, S. R. Marder, R. H. Friend, S. M. Menke, *ACS Nano* **2017**, *11*, 12473.
[32] J. H. Hou, O. Inganas, R. H. Friend, F. Gao, *Nat. Mater.* **2018**, *17*, 119.
[33] P. Cheng, G. Li, X. W. Zhan, Y. Yang, *Nat. Photon.* **2018**, *12*, 131.
[34] J. Z. Yao, T. Kirchartz, M. S. Vezie, M. A. Faist, W. Gong, Z. C. He, H. B. Wu, J. Troughton, T. Watson, D. Bryant, J. Nelson, *Phys. Rev. Appl.* **2015**, *4*, 014020.
[35] B. P. Rand, D. P. Burk, S. R. Forrest, *Phys. Rev. B* **2007**, *75*, 115327.
[36] M. Azzouzi, J. Yan, T. Kirchartz, K. K. Liu, J. L. Wang, H. B. Wu, J. Nelson, *Phys. Rev. X* **2018**, *8*, 031055.
[37] T. R. Kafle, B. Kattel, T. Wang, W.-L. Chan, *J. Phys.: Condens. Matter* **2018**, *30*, 454001.
[38] D. P. Qian, Z. L. Zheng, H. F. Yao, W. Tress, T. R. Hopper, S. L. Chen, S. S. Li, J. Liu, S. S. Chen, J. B. Zhang, X. K. Liu, B. W. Gao, L. Q. Ouyang, Y. Z. Jin, G. Pozina, I. A. Buyanova, W. M. Chen, O. Inganas, V. Coropceanu, J. L. Bredas, H. Yan, J. H. Hou, F. L. Zhang, A. A. Bakulin, F. Gao, *Nat. Mater.* **2018**, *17*, 703.
[39] Y. Liu, L. J. Zuo, X. L. Shi, A. K. Y. Jen, D. S. Ginger, *ACS Energy Lett.* **2018**, *3*, 2396.
[40] A. L. Ayzner, D. Nordlund, D. H. Kim, Z. N. Bao, M. F. Toney, *J. Phys. Chem. Lett.* **2015**, *6*, 6.
[41] Y. P. Yi, V. Coropceanu, J. L. Bredas, *J. Am. Chem. Soc.* **2009**, *131*, 15777.
[42] N. Sai, R. Gearba, A. Dolocan, J. R. Tritsch, W. L. Chan, J. R. Chelikowsky, K. Leung, X. Y. Zhu, *J. Phys. Chem. Lett.* **2012**, *3*, 2173.
[43] S. B. Jo, H. H. Kim, H. Lee, B. Kang, S. Lee, M. Sim, M. Kim, W. H. Lee, K. Cho, *ACS Nano* **2015**, *9*, 8206.
[44] B. P. Rand, D. Cheyns, K. Vasseur, N. C. Giebink, S. Mothy, Y. P. Yi, V. Coropceanu, D. Beljonne, J. Cornil, J. L. Bredas, J. Genoe, *Adv. Funct. Mater.* **2012**, *22*, 2987.
[45] V. Vohra, K. Kawashima, T. Kakara, T. Koganezawa, I. Osaka, K. Takimiya, H. Murata, *Nat. Photon.* **2015**, *9*, 403.
[46] T. Wang, T. R. Kafle, B. Kattel, Q. F. Liu, J. Wu, W. L. Chan, *Sci. Rep.* **2016**, *6*, 28895.
[47] W. Chen, H. Huang, S. Chen, Y. L. Huang, X. Y. Gao, A. T. S. Wee, *Chem. Mater.* **2008**, *20*, 7017.
[48] S. Duhm, G. Heimel, I. Salzmann, H. Glowatzki, R. L. Johnson, A. Vollmer, J. P. Rabe, N. Koch, *Nat. Mater.* **2008**, *7*, 326.
[49] M. Schwarze, W. Tress, B. Beyer, F. Gao, R. Scholz, C. Poelking, K. Ortstein, A. A. Gunther, D. Kasemann, D. Andrienko, K. Leo, *Science* **2016**, *352*, 1446.
[50] X. Y. Zhu, *J. Phys. Chem. Lett.* **2014**, *5*, 2283.
[51] Y. Ozawa, Y. Nakayama, S. Machida, H. Kinjo, H. Ishii, *J. Electron. Spectrosc. Relat. Phenom.* **2014**, *197*, 17.
[52] T. Wang, W. L. Chan, *J. Phys. Chem. Lett.* **2014**, *5*, 1812.
[53] D. R. T. Zahn, G. N. Gavrila, M. Gorgoi, *Chem. Phys.* **2006**, *325*, 99.
[54] T. R. Kafle, B. Kattel, S. D. Lane, T. Wang, H. Zhao, W. L. Chan, *ACS Nano* **2017**, *11*, 10184.
[55] T. Wang, Q. F. Liu, C. Caraiani, Y. P. Zhang, J. Wu, W. L. Chan, *Phys. Rev. Appl.* **2015**, *4*, 014016.
[56] T. R. Kafle, B. Kattel, P. Yao, P. Zereshki, H. Zhao, W. L. Chan, *J. Am. Chem. Soc.* **2019**, *141*, 11328.
[57] P. K. Watkins, A. B. Walker, G. L. B. Verschoor, *Nano Lett.* **2005**, *5*, 1814.
[58] B. Kattel, L. Qin, T. R. Kafle, W. L. Chan, *J. Phys. Chem. Lett.* **2018**, *9*, 1633.
[59] F. Iwatsu, T. Kobayashi, N. Uyeda, *J. Phys. Chem.* **1980**, *84*, 3223.
[60] A. A. Kocherzhenko, D. Lee, M. A. Forsuelo, K. B. Whaley, *J. Phys. Chem. C* **2015**, *119*, 7590.
[61] H. Bassler, A. Kohler, *PCCP* **2015**, *17*, 28451.
[62] D. Fazzi, M. Barbatti, W. Thiel, *J. Phys. Chem. Lett.* **2017**, *8*, 4727.
[63] J. Yuan, Y. Q. Zhang, L. Y. Zhou, G. C. Zhang, H. L. Yip, T. K. Lau, X. H. Lu, C. Zhu, H. J. Peng, P. A. Johnson, M. Leclerc, Y. Cao, J. Ulanski, Y. F. Li, Y. P. Zou, *Joule* **2019**, *3*, 1140.

[64] L. X. Meng, Y. M. Zhang, X. J. Wan, C. X. Li, X. Zhang, Y. B. Wang, X. Ke, Z. Xiao, L. M. Ding, R. X. Xia, H. L. Yip, Y. Cao, Y. S. Chen, *Science* **2018**, *361*, 1094.
[65] G. Giovannetti, G. Brocks, J. van den Brink, *Phys. Rev. B* **2008**, *77*, 035133.
[66] S. Saito, A. Oshiyama, *Phys. Rev. Lett.* **1991**, *66*, 2637.
[67] H. Jiang, J. Ye, P. Hu, F. X. Wei, K. Z. Du, N. Wang, T. Ba, S. L. Feng, C. Kloc, *Sci. Rep.* **2014**, *4*, 7573.
[68] J. E. Norton, J. L. Bredas, *J. Chem. Phys.* **2008**, *128*, 034701.

Supporting Information

Spontaneous exciton dissociation at organic semiconductor interfaces facilitated by the orientation of the delocalized electron-hole wavefunction

Tika R. Kafle,[1] Bhupal Kattel,[1] Shanika Wanigasekara,[1] Ti Wang,[2] Wai-Lun Chan[1, *]

[1] Department of Physics and Astronomy, University of Kansas, Lawrence, KS 66045

[2] School of Physics and Technology, Center for Nanoscience and Nanotechnology, and Key Laboratory of Artificial Micro- and Nano-structures of Ministry of Education, Wuhan University, Wuhan 430072, China

[*] Corresponding author: wlchan@ku.edu

I. Ionization Potential and Molecular Orientation

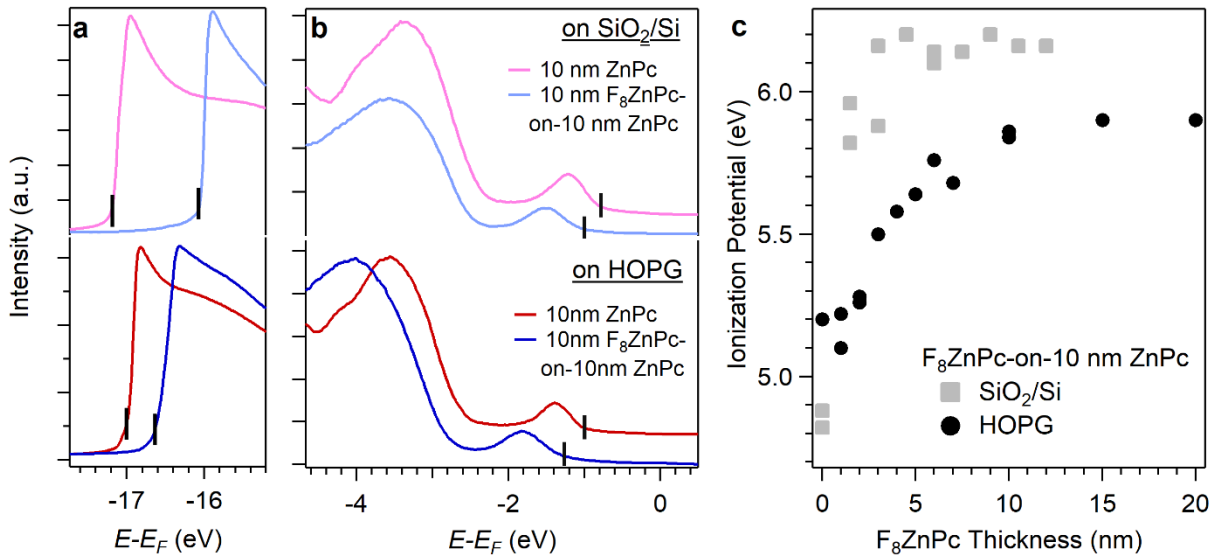

Figure S1. UPS spectra of 10 nm ZnPc, and 10 nm-F_8ZnPc/10 nm-ZnPc films grown on HOPG (lower) and SiO_2/Si (upper). Panel (a) shows the UPS spectra near the SECO region and panel (b) shows the same set of spectra near the HOMO region. The spectra were collected with the He-I emission line (photon energy = 21.22 eV). (c) The IP value as a function of F_8ZnPc thickness for F_8ZnPc on a 10 nm ZnPc layer. Data for the two different substrates, HOPG and SiO_2/Si, are shown in black and light-grey symbols, respectively.

It is known that the ionization potential (IP) of molecules such as phthalocyanine depends on its orientation (face-on and edge-on).[1-3] For example, the IP of CuPc, ZnPc, H_2Pc molecules with a face-on orientation are ~ 0.5 eV higher than that with an edge-on orientation. However, the opposite holds for fluorinated-Pc (e.g. F_8ZnPc),[2] i.e. the face-on orientation has a smaller IP than the edge on orientation. This is because the H-atoms, which have a low electronegativity, on the peripheral of the planar molecule are replaced by F-atoms, which have a high electronegativity. The IP can be determined readily by using ultraviolet photoemission spectroscopy (UPS). Figure S1a and S1b show the UPS spectra of 10 nm-ZnPc and 10 nm-F_8ZnPc/10 nm-ZnPc films deposited on SiO_2 (upper panel) and HOPG (lower panel). The UPS spectra near (a) the secondary electron cut off (SECO) region and (b) the HOMO region are shown. The photon energy subtracted by the energy difference between the SECO and the HOMO onset (marked by vertical bars) is equal to the IP. F_8ZnPc always has a higher IP than ZnPc, which is expected.[4]

Now, we can compare the IP value of the same molecules grown on different substrates (SiO_2/Si versus HOPG). For the 10-nm ZnPc film, the IP is 5.20 eV (red line) and 4.82 eV (pink

line) when it is deposited on HOPG and SiO_2/Si, respectively. These values are consistent with the IP for Pc molecules having a face-on and edge-on orientations.[1] Indeed, it is well-known that Pc molecules grow on HOPG and SiO_2 with a face-on and edge-on orientation, respectively.[1,2] We can further characterize the orientation of F_8ZnPc when it is grown on the ZnPc. Figure S1c shows that the IP of F_8ZnPc/10 nm-ZnPc grown on HOPG (black) and SiO_2/Si (light grey) as a function of F_8ZnPc thickness. At thickness = 0 nm, the sample is a 10 nm ZnPc film. The IP transitions to the IP value for the F_8ZnPc as the F_8ZnPc film becomes thicker. For thicknesses > 10 nm, the IP becomes steady and we use this value to determine the orientation of F_8ZnPc molecules. The IP value of the 10 nm-F_8ZnPc/10 nm-ZnPc/HOPG sample is 5.84 eV while the 10 nm-F_8ZnPc/10 nm-ZnPc/SiO_2 shows an IP of 6.16 eV. As discussed above, F_8ZnPc molecules with a face-on orientation should have a *smaller* IP than that with an edge-on orientation.[2,5] Hence, the F_8ZnPc molecule maintains the same orientation as the ZnPc molecule (face-on for HOPG and edge-on for SiO_2/Si) when it is deposited on ZnPc. Therefore, for the samples used in our TR-TPPE study, which were grown on HOPG, both ZnPc and F_8ZnPc molecules have a face-on orientation.

II. TR-TPPE spectra for samples with different F_8ZnPc thicknesses

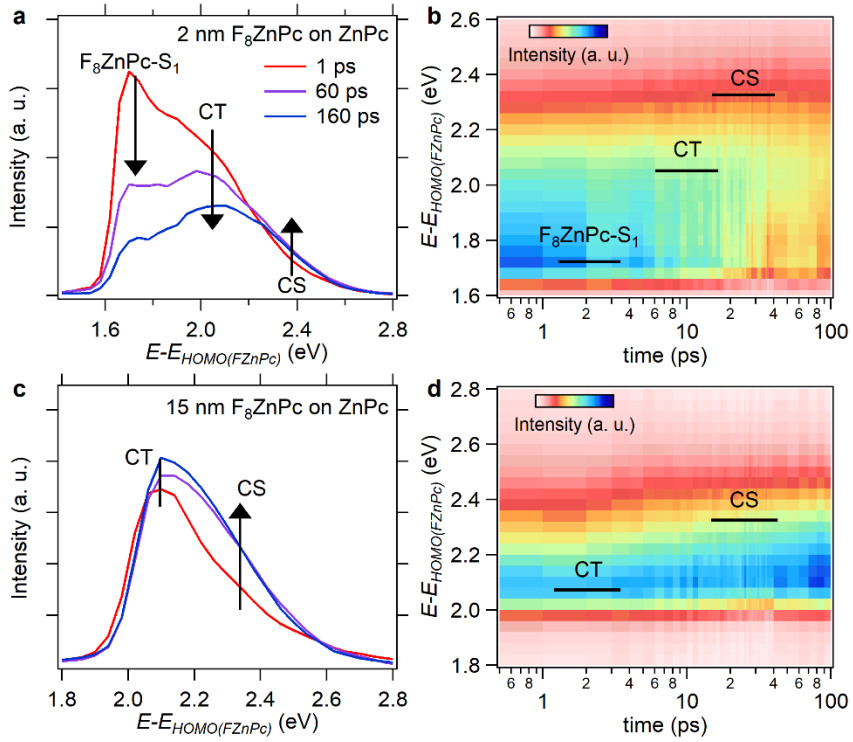

Figure S2. (a) TR-TPPE spectra of the 2 nm-F_8ZnPc/10 nm-ZnPc sample at selected delay times. (b) The two-dimensional plot of the TR-TPPE spectra for the same sample as (a). (c) TR-TPPE spectra of the 15 nm-F_8ZnPc/10 nm-ZnPc sample at selected delay times. (d) The two-dimensional plot of the TR-TPPE spectra for the same sample as (c).

For the 2 nm-F_8ZnPc/10 nm-ZnPc sample, the overlaying F_8ZnPc layer is thin. The signal is dominated by that originated from the interfacial CT state. The intensity growth of the CS state is not pronounced, which indicates that the ultrathin F_8ZnPc layer can prohibit charge separation by limiting the electron-hole separation. On the contrary, the intensity growth of the CS state is more pronounced in the 15 nm-F_8ZnPc/10 nm-ZnPc sample. Note that the absolute intensity is much weaker for the 15 nm sample as compared to the 2 nm sample (Fig. 3a in the main text). This indicates that both of these states are originated from the buried interface.

Morevoer, the workfunction of the 2 nm sample is lower than that of samples with a thicker F_8ZnPc layer. Hence, deeper states such as the F_8ZnPc's S_1 state can be observed. The F_8ZnPc's S_1 state has a shorter lifetime as compared to the CT state. This is expected because hole transfer from F_8ZnPc to ZnPc will quench the F_8ZnPc's S_1 state. Moreover, no state at an energy lower than the CT state has a lifetime longer than that of the CT state. Hence, we do not observe the relaxation of the CT exciton into other lower energy states.

III. Temperature and Fluence Dependences of the SED Process

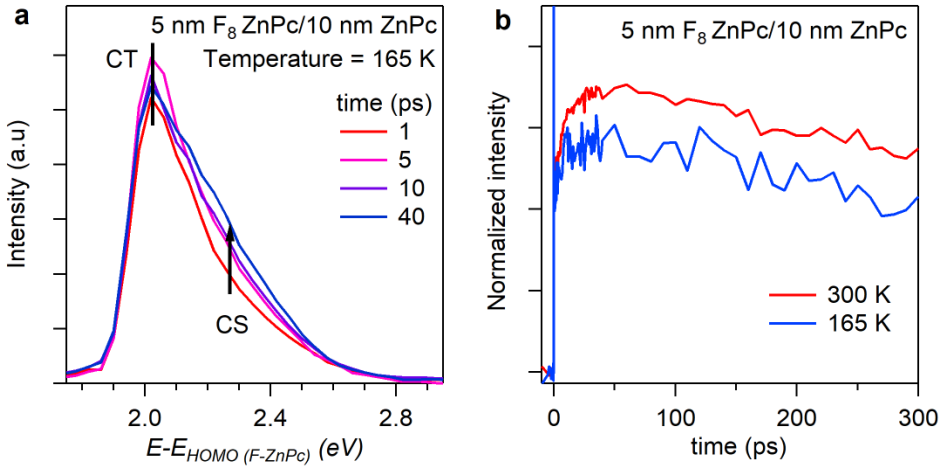

Figure S3. (a) TR-TPPE spectra at selected pump-probe delay times for the 5 nm-F_8ZnPc/10 nm-ZnPc sample taken at 165 K. The upward arrow indicates the position of the CS states at which the intensity is increasing as the time increases. (b) A comparison of the CS state dynamic at 165 K (blue) and 300 K (red). For comparison, the intensity is normalized at $t = 0$ ps.

Experiments were also performed at lower temperatures for the 5 nm F_8ZnPc/10 nm ZnPc sample. The TR-TPPE spectra obtained at 165 K is shown in Fig. S3a. Similar to the spectra taken at the room temperature (Fig. 2 in the main text), both the CT and CS states can be identified. Moreover, an increase in the intensity in the spectral range corresponding to the CS state is observed. The dynamics of the intensity near the spectra range of the CS state at two different temperatures is shown in Fig. S3b. Compared to the measurement taken at 300 K, the magnitude of the intensity growth is slightly weaker at 165 K, but the dynamics is similar. Hence, we conclude that the SED process can still occur at 165 K.

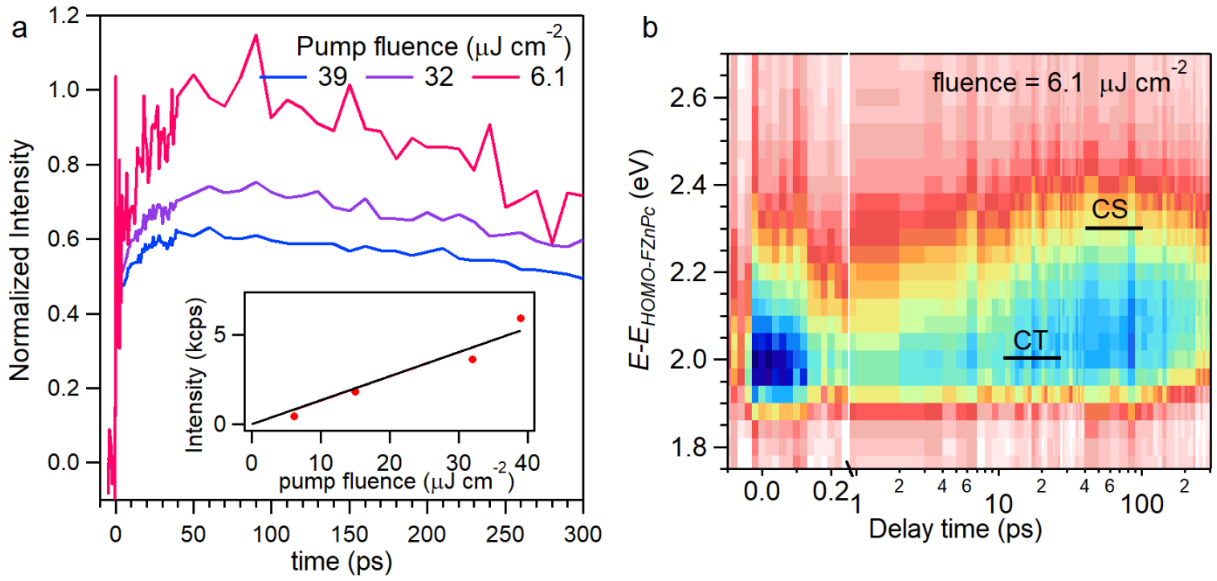

Figure S4. (a) The CS state dynamics for various pump fluences. Inset - The signal intensity at time zero as a function of pump fluence. (b) The TR-TPPE spectrum at the lowest pump fluence. The shift of the spectral weight towards the higher energy is clearly observed.

Experiments were performed at various pump fluences (6.1 – 39 μJ cm^{-2}) for the 5 nm F_8ZnPc/10 nm ZnPc sample. The evolution of intensity at the CS peak is shown in Fig. S4a. The intensity is normalized by the intensity at time zero. As expected, the intensity at time zero scales linearly with the pump fluence (inset of Fig. S4a). The growth in the CS intensity is more pronounced at lower fluences. Fig. S4b shows the full TR-TPPE spectrum at the lowest fluence used in our experiment. The energy upshift in the spectral weight is clearly observed. Hence, the energy uphill SED is not induced by non-linear Auger-like processes because it is more apparent at lower fluences. On the other hand, the SED process is somewhat suppressed at higher fluences, which can be attributed to the lowering of the CS yield due to exciton-exciton annihilation.

IV. Electron Transfer from ZnPc to F_8ZnPc

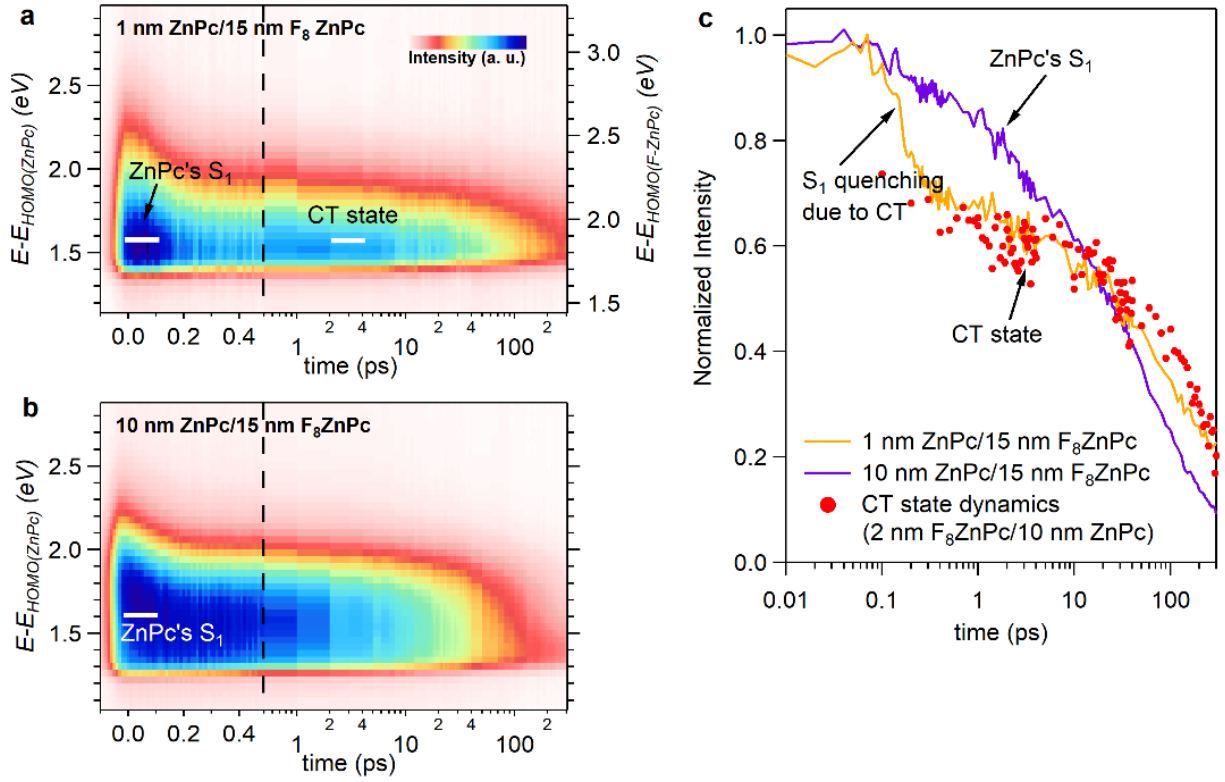

Figure S5. (a) The TR-TPPE spectrum of the 1 nm-ZnPc on 15 nm-F_8ZnPc sample. The spectrum is split into two halves (indicated by the dashed line) in order to show dynamics on different timescales. (b) The TR-TPPE spectrum of the 10 nm-ZnPc on 15 nm-F_8ZnPc sample. (c) The intensity evolution at the spectral range near the ZnPc's S_1 for the two samples shown in (a) and (b). The red dots represent the dynamics of the CT state for the 2 nm-F_8ZnPc on ZnPc sample (Figure S2a).

In order to observe electron transfer from ZnPc to F_8ZnPc, we deposited the ZnPc layer on top of the F_8ZnPc layer. Because TPPE is a surface sensitive probe, flipping the order of the two layers allows us to detect the ZnPc's S_1 with a better clarity. Figure S5a and b show the TR-TPPE spectra for the 1 nm-ZnPc/15 nm-F_8ZnPc sample and the 10 nm-ZnPc/15 nm-F_8ZnPc sample, respectively. For the 10 nm-ZnPc sample, only the ZnPc's S_1 is observed (Fig. S5b). In accordance with our previous studies,[6,7] this state is appeared at ~ 1.6 eV above the ZnPc's HOMO. At these thicknesses, the photoemission intensity, which represents the population of S_1 exciton near the surface, is not affected significantly by the CT process that occurs at the buried interface.[6,7] On the other hand, for the 1 nm-ZnPc sample, the electron transfer from ZnPc to F_8ZnPc results in the quenching of the ZnPc's S_1 signal because the CT process reduces the ZnPc's S_1 population. Comparing Fig. S5a and S5b, such quenching can be observed at t ~ 0.1 – 0.3 ps after

photoexcitation. Figure S5c shows the decay of the ZnPc's S_1 intensity for the 10 nm-ZnPc sample (purple line) and the 1 nm-ZnPc sample (orange line). The purple curve essentially represents the intrinsic dynamics of the S_1 exciton in a standalone ZnPc film. For the orange curve, the intensity quenching on the 100 fs timescale can be clearly observed, which indicates that the electron transfer from ZnPc to F_8ZnPc occurs at ~ 100 fs after photoexcitation.

However, the intensity is not quenched all the way to zero. The residue intensity can be assigned to the interfacial CT state. With a 1 nm-ZnPc layer, it is possible to observe the CT exciton.[7,8] The energy of this peak is at ~ 1.8 – 1.9 eV above the F_8ZnPc's HOMO (the right axis in Fig. S5a), which is consistent with the position of the CT state observed with the F_8ZnPc-on-ZnPc samples (see Fig. 2 in the main text and Fig. S2). Moreover, the decay dynamics of the intensity (orange curve) coincides with the decay of the CT state intensity observed in the 2 nm F_8ZnPc-on-10 nm ZnPc sample (shown as red circles in Fig. S5c). This further supports our assignment. We also note that the CT state, which is an interlayer exciton, has a longer lifetime than the ZnPc's S_1 state (note that the *x*-axis is on a log scale).

V. Measurement for charge generation from the ZnPc/C_{60} interface

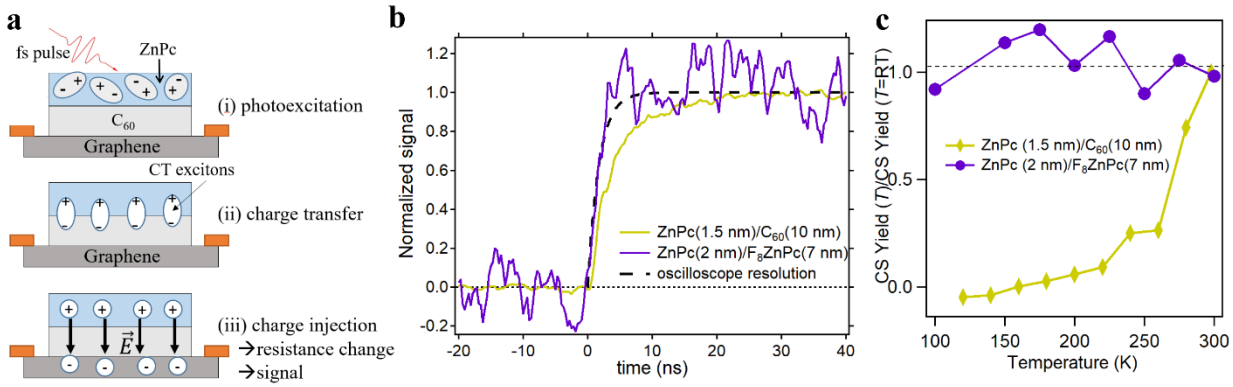

Figure S6. (a) A schematic diagram showing the principle of the TR-GFET method that we developed to measure the CT exciton dissociation dynamics and charge separation yield. (b) The charge generation dynamics from 1.5 nm ZnPc/10 nm C_{60} and 2 nm ZnPc/7 nm F_8ZnPc interfaces. The dashed line represents the instrumental response for our oscilloscope. For the ZnPc/F_8ZnPc sample, a 5 nm of PTCDA is inserted between graphene and the F_8ZnPc layer, which serves as a hole blocking layer to avoid direct quenching of F_8ZnPc's S_1 exciton at graphene. (c) The carrier generation yield as a function of temperature for a 1.5 nm ZnPc/10 nm C_{60} and a 2 nm ZnPc/7 nm F_8ZnPc sample. The data is obtained from the TR-GFET technique.

As mentioned in the main text, CT excitons were found to relax to its lower energy states at the ZnPc/C_{60} interface. These bound CT excitons were found to dissoicate in ~ 3.4 ns,[9,10] which was measured by a time-resolved photoelectrical measurement technique that uses graphene field effect transitor (GFET) to probe the amount of free carriers generated from the interface. The details and results of this work are reported in Ref. [9]. For convenient, the basic principle of this method is shown schematically in Fig. S6a. In the TR-GFET experiment, the ZnPc/C_{60} film is deposited on graphene. If free carriers are generated from the ZnPc/C_{60} interface, the free holes will remain trapped in the ZnPc layer, while free electrons can inject into graphene. The trapped holes in the topmost donor layer will create an E-field that induces electron doping in graphene (as in a parallel-plate capacitor). The electron doping modifies the conductivity of the graphene channel, which can be captured by the oscilloscope. Similar experiments can be carried for the ZnPc/F_8ZnPc interface. The measured signal as a function of time is shown in Fig. S6b. For the F_8ZnPc/ZnPc sample, the signal rise time is limited by the time resolution of our oscillscope. Hence, the result is consistent with the ~ 10 ps charge generation time orginated from the SED process observed in our TR-TPPE experiment. For the ZnPc/C_{60} interface, the signal rise is

delayed, which can be attributed to the slow thermal dissociation (a few ns) of the bound CT exciton.

In addition to the slow CT exciton dissoication time, we found that the charge separation yield depends heavily on the temperature for the ZnPc/C_{60} interface. Figure S6c shows the signal ampiltude, which is proportional to amount of separated carriers, as a function of temperature. The signal amplitude is normalized by the amplitude at the room temperature. The amount of separated carriers decrease rapidly as the temperature decreases. This indicates that the charge separation process is thermal activated. On the other hand, the charge generation yield at the F_8ZnPc/ZnPc interface is almost independent of the temperature. This weak temperature dependence can be explained by the much faster SED rate as compared to the CT exciton recombination rate at the full temperature range. Hence, it implies a weak temperature dependence of the SED rate.

VI. Additional data from the tight binding model

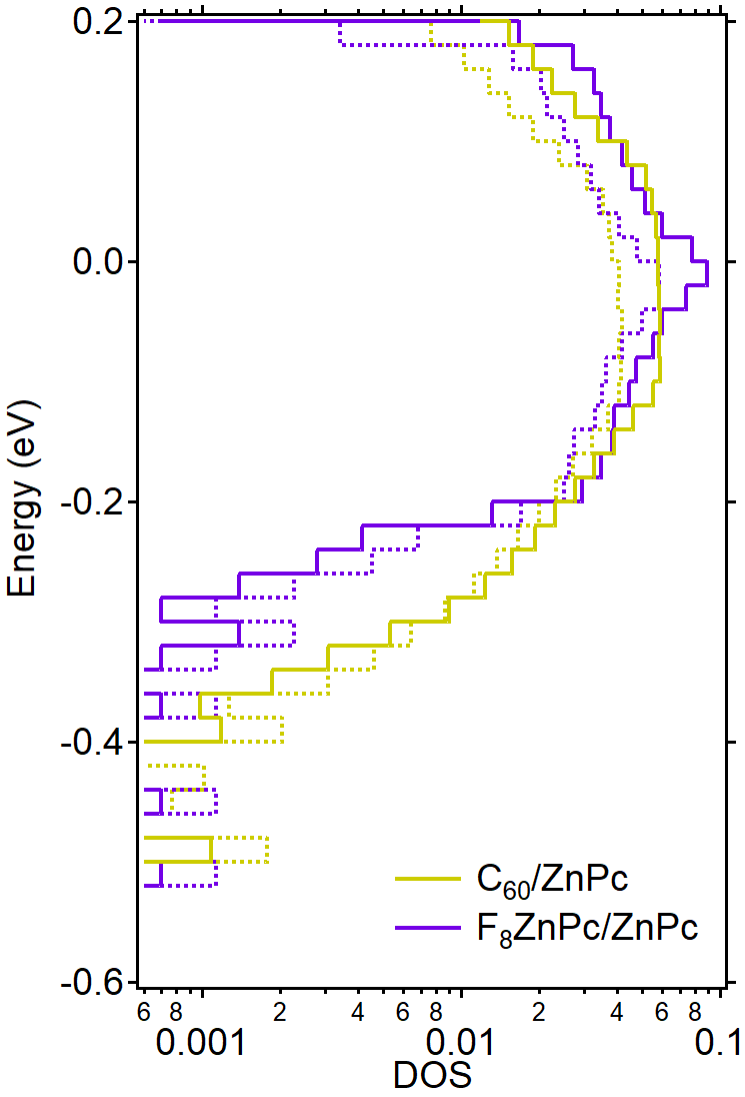

Figure S7. The nomalized DOS as a function of energy calculated with a simulation size of 15 nm (solid line) and 10 nm (dashed line). To directly compare the slope of the DOS curves, the normalized DOS for the 15 nm case is multipled by a factor of 0.7. Since the DOS (*x*-axis) is plotted in a log scale, multipying it with a constant factor only shifts the curve horizontally, but does not change the slope.

The major effect of increasing the cell size from 10 nm to 15 nm is an increase in the number of the band-like charge separated states. It does not have any strong effect on CT states as the Coulumb interaction is very weak for separation > 10 nm. Hence, the slope of the DOS curve near the region corresponding the CT states (energy ~ -0.2 – -0.5 eV) is not affected.

VII. More details for the tight binding model

When the Hamiltonian in the main text is diagonalized, an eigenstate with the index k is expressed as:

$$\Psi_k = \sum_{i,j} a_{i,j}(k)|i,j\rangle$$

The state $|i,j\rangle$ represents the electron and hole locate in the site i in the acceptor crystal and site j in the donor crystal, respectively. Hence, the electron-hole distance r_{ij} of $|i,j\rangle$ can be determined readily under this site representation. Then, the average electron-hole distance r_k for the eigenstate ψ_k is given by:

$$r_k = \sum_{i,j} \left|a_{i,j}(k)\right|^2 r_{i,j}$$

To calculate the electron and hole densities $\rho(i)$ and $\rho(j)$ that are shown in Fig. 5c in the main text, the electron density at site i in the acceptor crystal is given by:

$$\rho_k(i) = \sum_{j} \left|a_{i,j}(k)\right|^2$$

Similarly, the hole density at site j in the donor crystal is given by:

$$\rho_k(j) = \sum_{i} \left|a_{i,j}(k)\right|^2$$

References:

1 Wang, T. *et al.* Growing Ultra-flat Organic Films on Graphene with a Face-on Stacking via Moderate Molecule-Substrate Interaction. *Scientific Reports* **6** (2016).

2 Chen, W. *et al.* Molecular orientation-dependent ionization potential of organic thin films. *Chemistry of Materials* **20**, 7017-7021 (2008).

3 Duhm, S. *et al.* Orientation-dependent ionization energies and interface dipoles in ordered molecular assemblies. *Nat Mater* **7**, 326-332 (2008).

4 Schwarze, M. *et al.* Band structure engineering in organic semiconductors. *Science* **352**, 1446-1449 (2016).

5 Chen, W. *et al.* Molecular orientation dependent energy level alignment at organic− organic heterojunction interfaces. *The Journal of Physical Chemistry C* **113**, 12832-12839 (2009).

6 Wang, T., Kafle, T. R., Kattel, B. & Chan, W.-L. A multidimensional view of charge transfer excitons at organic donor–acceptor interfaces. *Journal of the American Chemical Society* **139**, 4098-4106 (2017).

7 Kafle, T. R. *et al.* Charge Transfer Exciton and Spin Flipping at Organic–Transition-Metal Dichalcogenide Interfaces. *ACS nano* **11**, 10184-10192 (2017).

8 Kafle, T. R. *et al.* Effect of the Interfacial Energy Landscape on Photo-induced Charge Generation at the ZnPc-MoS2 Interface. *Journal of the American Chemical Society* **141**, 11328-11336 (2019).

9 Kattel, B., Qin, L., Kafle, T. R. & Chan, W.-L. Graphene Field-Effect Transistor as a High-Throughput Platform to Probe Charge Separation at Donor–Acceptor Interfaces. *The journal of physical chemistry letters* **9**, 1633-1641 (2018).

10 Kafle, T. R., Kattel, B., Wang, T. & Chan, W.-L. The relationship between the coherent size, binding energy and dissociation dynamics of charge transfer excitons at organic interfaces. *J. Phys.: Condens. Matter* **30**, 454001 (2018).